ROYAL SOCIETY OF CHEMISTRY

PAPER

Check for updates

Adsorption properties of α-type layered and pillared zirconium phosphite phosphonates with high specific surface areas and porosities

Monica Pica, [ID] *[a] Elena De Paolis,[a] Emmanuele Cillo,[a] Giorgio Gatti, [ID] [b]
Geo Paul, [ID] [c] Elisa Calà,[b] Fabrizio Olivito, [ID] [d] Anna Santaniello[d] and
Giovanni Golemme [ID] [d,e,f]

Single-phase mixed zirconium phosphite phosphonates with layered and pillared structures were prepared by direct reaction of a zirconyl salt and phosphorous acid with phenylphosphonic or *p*-xylenediphosphonic acid, respectively. Materials with different chemical compositions were prepared by changing the phosphorous acid/phosphonic acid molar ratio in the mother solution between 1 and 4. The compounds were characterised by XRPD, ^{31}P MAS NMR, SEM, and FTIR analyses. The adsorption/desorption properties toward nitrogen and hydrogen at 77 K and the dichloromethane (DCM) uptake from the vapor phase at 30 °C were studied. All materials exhibited a Specific Surface Area (SSA) of ≥ 200 m^2 g^{-1}, due to the contribution of micro-, meso- and macropores. The estimated micropore volume, V_{micro}, increased with increasing SSA and affected the hydrogen uptake that reached 1.43 mmol g^{-1} at 77 K with the zirconium phosphite phenylphosphonate compound having the highest V_{micro} value. The DCM uptake reached 1300 mg g^{-1} with the zirconium phosphite *p*-xylenediphosphonate having the highest macroporosity. The zirconium phosphite phenylphosphonate in the gel form was proved to disperse well in a PLA matrix, even at high filler loadings, affecting its physico-chemical properties.

1. Introduction

Metal(IV) phosphonates have had a glorious past since 1978 when they were first synthesized by Alberti and Costantino.[1] More recently, a step forward has been taken, with the discovery of nanocrystalline α-type zirconium phosphate (nano-ZrP) and of a new synthetic approach, the so-called gel method.[2] It was found that, due to its higher reactivity with respect to the corresponding microcrystalline material, nanocrystalline ZrP is able to react with phosphonic acids by topotactic anion exchange reactions, thus obtaining single-phase mixed zirconium phosphate phosphonate compounds.[3,4] Moreover, the same compounds can also be obtained by direct synthesis through the gel method, which is also used for the synthesis of nano-ZrP.[3] A key

aspect of this method is that it is easy, since all syntheses are carried out generally at room temperature or at 80 °C without using complexing agents, such as HF. The versatility of the method is due to the use of an uncommon Zr(IV) salt, that is zirconyl propionate; differently from zirconyl chloride, the propionate group makes it soluble in organic solvents and, at the same time, acts as a better complexing agent toward zirconium and is a worse leaving group than chloride, thus allowing it to slow down the reaction between Zr(IV) and phosphoric/phosphonic acids. Furthermore, the use of aliphatic alcohols as solvents during synthesis allows direct solvent intercalation, with an enlargement and, in turn, more favoured access to the interlayer region with respect to not-intercalated ZrP.

In light of the above observations and of the huge amount of work done in the more and less recent past in the chemistry of metal layered phosphonates, the question is: is it worthwhile to continue studying this class of compounds? The answer is, of course, yes, for several reasons: first, the commercial availability of new phosphonic acids enables the synthesis of new functional materials; second, easier access to more accurate characterization techniques provides better comprehension of the characteristics and properties of known compounds; and last but not least, application of the gel method to the synthesis of known materials could pave the way to new properties and applications.

[a]Department of Pharmaceutical Sciences, Perugia University, Via del Liceo 1, 06123 Perugia, Italy. E-mail: monica.pica@unipg.it
[b]Department for Sustainable Development and Ecological Transition, University of Eastern Piedmont 'Amedeo Avogadro', Piazza Sant' Eusebio 5, 13100 Vercelli, Italy
[c]Department of Sciences and Technological Innovation, University of Eastern Piedmont 'Amedeo Avogadro', Viale T. Michel 11, 15121 Alessandria, Italy
[d]Department of Environmental Engineering, University of Calabria, Via P. Bucci 45A, 87036 Rende, Italy
[e]LPM Lab, STAR Research Infrastructure, Via Tito Flavio, University of Calabria, 87036 Rende, Italy
[f]INSTM Consortium, Calabria Section, University of Calabria, 87036 Rende, Italy

The present paper reports, for the first time, application of the gel method for the synthesis of nanosized α-type zirconium phosphonates with significant specific surface areas and porosities. Both Alberti and Clearfield explored the use of phosphonate building blocks of different sizes as Zr(IV) ligands in order to improve the specific surface area and micro- and mesoporosity.[5–8] These compounds were generally prepared in ethanol, DMSO or their mixtures by the reaction of phosphoric acid (or phosphorous acid) and phosphonic acid (or diphosphonic acid) with ZrF_6^{2-}. This represents an extension of the previous work, since the gel method allows the easier preparation of the above compounds with variable compositions and without using additional complexing agents. Among other things, the possibility of obtaining these materials in the form of a gel, containing loosely aggregated particles, is advantageous for their dispersion in a polymeric matrix, promoting more intimate contact between the two phases. With this aim, two different phosphonic acids, phenylphosphonic acid and *para*-xylenediphosphonic acid, were used together with phosphorous acid to obtain mixed zirconium phosphite phosphonates. Material characterization was carried out by ^{31}P MAS NMR, X-ray diffraction analysis and scanning electron microscopy. Finally, N_2 and H_2 adsorptions at 77 K were reported, together with dichloromethane adsorption at 293 K. Their use as fillers in a polymeric matrix was also investigated.

2. Experimental

2.1. Reagents

Zirconyl propionate ($ZrO_{1.27}(C_2H_5COO)_{1.46}$, MW = 218 Da) was kindly supplied by MEL Chemicals, England. *para*-Xylenediphosphonic acid (labelled as H_4P2) was supplied by TCI Europe. Phenylphosphonic acid (labelled as H_2P1) and all other reagents were supplied by Merck KGaA and used as received, without further purification.

2.2. Synthesis of zirconium phosphite phenylphosphonate and zirconium phosphite *p*-xylenediphosphonate materials

A weighted amount of zirconyl propionate was dissolved in 6 mL of propanol. Separately, weighed amounts of phosphorous acid and H_2P1 or H_4P2 were dissolved in 6 mL of propanol. When H_4P2 was used, a milky suspension was obtained. In all experiments, the total phosphorous/Zr molar ratio was 4. The second solution was added to the first one, thus obtaining gelatinous precipitates that were left at 80 °C in an oven for 24 hours. The precipitates were then centrifuged and washed

twice with propanol, and finally dried in an oven at 60 °C overnight. Hereafter, zirconium phosphite phenylphosphonate solids will be labelled as ZrP1$_y$_R and zirconium phosphite *p*-xylenediphosphonate solids will be labelled as ZrP2$_y$_R, where *y* is the number of phosphonate groups per mol of zirconium and *R* is the $H_3PO_3/H_2P1(H_4P2)$ molar ratio employed in the synthesis.

For more general discussions, the above material will be generically labelled as ZrP*n*, with *n* = 1, 2. Table 1 reports the amounts of reagents used in the various syntheses.

2.3. Techniques

Powder X-ray diffraction (XRD) patterns were obtained using a Bruker D8 Advance diffractometer (Bruker AXS GmbH, Karlsruhe, Germany) equipped with a Lynxeye XE-T detector using a Cu-Kα radiation source. A long fine focus (LFF) tube was operated at 40 kV and 40 mA, with a step size of 0.033° and a step scan of 30 s. Powder samples were side loaded onto a glass sample holder.

SEM analysis was performed using a Zeiss LEO 1525 FE scanning electron microscope in the Department of Physics and Geology of Perugia University. The powder samples were placed onto an aluminum stub precoated with a double-sided adhesive conductive carbon tape and vacuum metalized for applying a chromium coating.

The P and Zr contents were determined using a Varian Liberty inductively coupled plasma–optical emission spectrometer (ICP-OES) with axial injection. About 15 mg of the powder samples was dissolved by treatment with 3 M HF (~0.15 mL), and then the solutions were diluted by adding 10^{-3} M HNO_3.

Solid-state NMR spectra were obtained using a wide bore 11.75 Tesla magnet and a Bruker Avance III 500 spectrometer with operational frequencies for ^{1}H and ^{31}P of 500.13 and 202.46 MHz, respectively. A 4 mm triple resonance probe, in double resonance mode, with magic angle spinning (MAS) was employed in all the experiments, and the samples were packed in a zirconia rotor and spun at a MAS rate of 15 kHz. [31]P MAS spectra were obtained with a 90° pulse, and the magnitude of the radio frequency field was 71 kHz with ^{1}H decoupling during acquisition. Spectra were recorded with a spectral width of 100 kHz, and 16 transients were accumulated at 300 K using a relaxation delay between accumulations of 300 s. All chemical shifts are reported using the δ scale and are externally referenced to ammonium dihydrogen phosphate at 0.8 ppm for ^{31}P NMR.

Table 1 Amounts of reactants used in each synthesis

Phosphonic acid	Zr (mmol)	H_3PO_3 (mmol)	Phosphonic acid (mmol)	H_3PO_3/Zr molar ratio	H_3PO_3/H_2P1(H_4P2) molar ratio (R)
H_2P1	3.53	7.06	7.06	2	1
	3.53	8.50	5.65	2.4	1.5
	3.53	10.6	3.53	3.0	3.0
H_4P2	3.53	8.50	2.83	2.4	3.0
	3.53	9.08	2.52	2.6	3.6

Nitrogen and hydrogen physisorption measurements were performed using a Tristar 3020 II BET surface area analyzer (Micromeritics, Norcross, GA, USA) at 77 K. A known amount of zirconium phosphite phosphonate was introduced into the sample tube and degassed by heating at 150 °C in a flux of dry nitrogen. All gases (SIAD, Bergamo, Italy) were 99.999% pure.

Thermogravimetric measurements were carried using a Discovery SDT 650 thermal analyzer (TA Instruments, New Castle, DE, USA) at a heating rate of 10 °C min^{-1} under air flow (100 cc min^{-1}).

Infrared spectroscopy analyses were performed using a Nicolet IS50 (Thermo Fisher Scientific, Waltham, MA, USA) spectrometer, featuring 64 scans and a resolution of 4 cm^{-1} over a spectral range of 4000–400 cm^{-1}. The samples were analyzed under vacuum conditions using an IR cell equipped with KBr windows, attached to a vacuum line, that maintained a residual pressure of $\leq 5 \times 10^{-4}$ mbar.

Dichloromethane (DCM) uptake was evaluated using a desiccator containing a vessel filled with liquid dichloromethane and a filter holder loaded with a weighed amount of the material previously dried at 100 °C for 1 hour in an oven. All measurements were conducted at 30 °C and atmospheric pressure. At regular time intervals, the sample was weighed, and the amount of dichloromethane absorbed was determined by calculating the difference between the weight at time t and the initial weight. In the calculation, the absorption of water vapor present inside the vessel was considered negligible. The amount of DCM taken up at a given time was calculated according to the following equation:

$$\text{DCM mass} = \frac{m_{\text{ZrP}n} - m^{\circ}_{\text{ZrP}n}}{m^{\circ}_{\text{ZrP}n}}$$

where $m_{\text{ZrP}n}$ is the mass of ZrPn after equilibration with DCM and $m^{\circ}_{\text{ZrP}n}$ is the mass of the dried sample.

3. Results and discussion

In the present work, zirconium phosphite phosphonates were synthesised for the first time by using the gel method. Two different phosphonic acids were used in combination with phosphorous acid: phenylphosphonic acid and p-xylenediphosphonic acid, as reported in Table 1. ^{31}P MAS NMR analysis was carried out in order to get information about the connectivity of phosphorus groups with zirconium. In Fig. 1, two representative NMR spectra are shown.

The two main signals in spectrum (a) observed at −18.2 and −5.6 ppm, related to ZrP1$_y$_1.5, are assigned, according to the literature, to the phosphite and phenylphosphonate groups, respectively, bound through the oxygens to three Zr(IV) atoms, as typically occurs in the α-type structure.[9] The zoomed ^{31}P NMR spectra, recorded in MAS and CPMAS modes, highlight the presence of weak signals at around 3.8 ppm, 11 ppm and 18.2 ppm that are assigned to doubly bonded, singly bonded and non-bonded phenylphosphonate groups, respectively (Fig. S1A, SI). This is in agreement with other works according to which the phosphate or
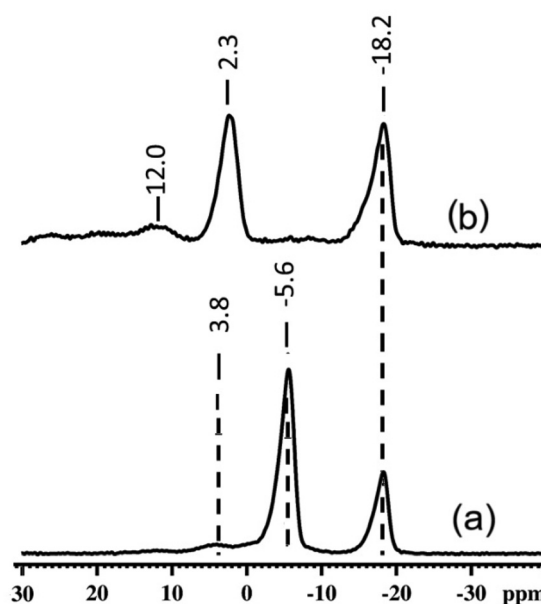

Fig. 1 ^{31}P MAS NMR spectra of ZrP1$_y$_1.5 (a) and ZrP2$_y$_3.0 (b).

phosphonate groups with connectivity values less than three are generally shifted toward higher chemical shifts.[2,9]

Similar assignments can be done on ZrP2$_y$_3.0 (Fig. 1b) where the main resonance of the triply coordinated diphosphonate lies at around 2.3 ppm. The zoomed ^{31}P NMR spectra recorded in MAS and CPMAS modes, shown in Fig. S1B, SI, showed very weak signals at 11.9, 19.2 and 26.3 ppm due to doubly bonded, singly bonded and non-bonded phosphonate groups, respectively.

As reported in previous works,[2,10,11] the low connectivity phosphate groups can be located at the edge and corners of the layers and their contribution becomes more significant as the particle size is reduced.

However, the contribution due to poorly connected phosphonate groups does not compromise the prevalent formation of the α-type layer structure, due to the strong tendency of Zr(IV) to form highly stable layered phosphonate compounds, even in the presence of a certain number of phosphonate groups not connected through three oxygen atoms.

Similar qualitative results were obtained for all compounds. Moreover, NMR spectra allowed estimation of the phosphonate to phosphite molar ratios for the various compounds. By considering that the total phosphorous/Zr molar ratio, determined by ICP analysis, is close to 2 for all samples (see Table 2), the

Table 2 Composition of the ZrPn_y_R materials

Phosphonic acid	P/Zr	x	y	Sample label
H$_2$P1	2.01	0.3	1.7	ZrP1$_{1.7}$_1.0
	1.99	0.5	1.5	ZrP1$_{1.5}$_1.5
	1.98	0.8	1.2	ZrP1$_{1.2}$_3.0
H$_4$P2	2.02	1.0	0.5	ZrP2$_{0.5}$_3.0
	1.99	1.2	0.4	ZrP2$_{0.4}$_3.6

following general chemical composition can be assigned to the compounds:

$$Zr(O_3PH)_x(\textbf{P}\textbf{n})_y$$

where

$$y = 2 - x \text{ for } Zr\textbf{P1}_y\_R$$

$$y = 1 - x/2 \text{ for } Zr\textbf{P2}_y\_R$$

The chemical compositions of all materials are reported in Table 2.

In order to get information about the affinity of the phosphonates and phosphite toward Zr(IV), the amount of phosphorous acid per mol of zirconium in the mother solution before precipitation was plotted against the phosphite/Zr molar ratio in the corresponding solid and the results are shown in Fig. 2. In the same plot, three straight lines are also reported, representing the theoretical composition of the solids, by assuming a much higher affinity (red dashed line), a much lower affinity (blue dashed line) and the same affinity (black dashed line), toward Zr(IV), of the phosphite with respect to the phosphonates.

For all the Zr**P1**$_y$_R samples, the experimental points (black circles) lie very close to the blue line, suggesting that the phenylphosphonate has a higher affinity than the phosphite for Zr; differently, the chemical composition of Zr**P2**$_y$_R samples (red triangles) is closer to that expected by assuming similar affinities of the diphosphonate and phosphite for Zr. This information is quite important in order to select the most suitable experimental conditions for the synthesis of the desired compounds.
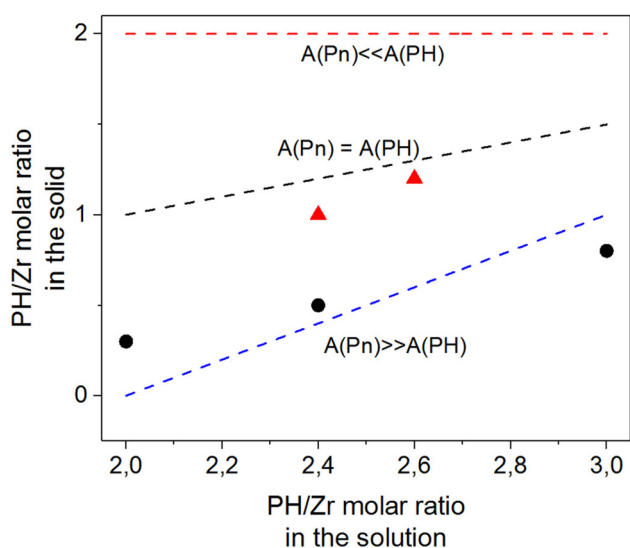
The plot in Fig. 3, representing the (phosphite/phosphonate) molar ratio in the solids (x/y) *versus* the phosphorous/phosphonic acid molar ratio in the reaction mixture (R), shows that all the experimental points lay below the straight line corresponding to $x/y = R$, which is in agreement with the higher affinity of phosphonic acids toward Zr(IV) with respect to phosphorous acid; among them, comparing the samples with $R = 3.0$ shows that the phenylphosphonic acid is preferred with respect to the diphosphonic acid.

However, giving an explanation of the different affinities of phosphonate ligands toward Zr(IV) is not trivial, since several aspects should be considered:

• the molecular structure of the ligands, in particular the electronic density of the PO_3H_2 moiety, which also depends on the nature of the substituents; in addition, it should be considered that the Zr–O–P bonds in such compounds are neither purely ionic nor covalent;

• the stability of the final solid compounds, which is difficult to evaluate, since the materials are neither crystalline with a regular structure nor pure compounds that are composed of one kind of ligand.

Fig. 4 shows the X-ray powder diffraction patterns of the Zr**P**n samples; they are typical of nanosized α-type single-phase mixed zirconium phosphonates with the different phosphorus groups interdispersed on the layer surface. Two facts are in support of this. (1) The interlayer distances of all materials, reported in the upper part of Fig. 4, lie between the interlayer distance of $Zr(O_3PH)_2$, 5.6 Å, and the interlayer distances of pure phosphonates, 14.8 Å for $Zr(O_3PPh)_2$ and 10.8 Å for $Zr(O_6P_2C_8H_8)$.[1] The formation of compounds with asymmetric layers, characterised by an alternation of interlayer regions richer in phosphite and others richer in phosphonate, can be reasonably excluded, since in this case, the interlayer distances
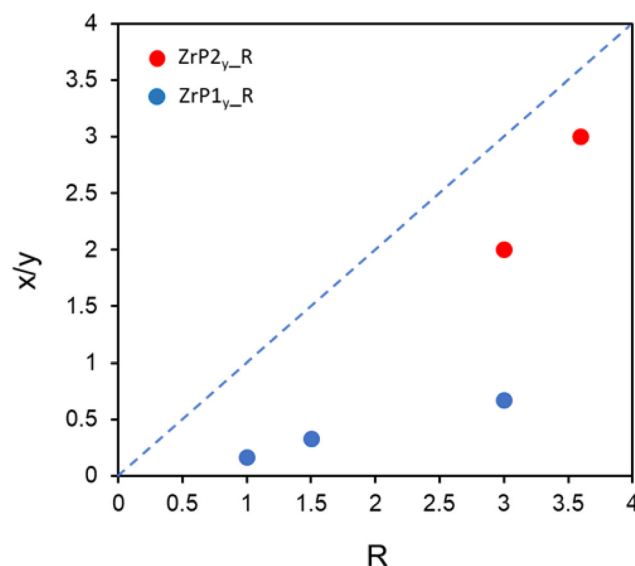

Fig. 2 Chemical composition of the solids as a function of the composition of the reaction solution for Zr**P1**$_{1.7}$_1.0, Zr**P1**$_{1.5}$_1.5 and Zr**P1**$_{1.2}$_3.0 (black circles) and Zr**P2**$_{0.5}$_3.0 and Zr**P2**$_{0.4}$_3.6 (red triangles). The dashed straight lines represent the theoretical solid compositions calculated by assuming very different or similar affinities of the phosphonates and phosphite groups for Zr(IV).

Fig. 3 The phosphite to phosphonate molar ratio in the solids (x/y) as a function the phosphorous/phosphonic acid molar ratio in the reaction mixture (R) for the Zr**P**n samples.
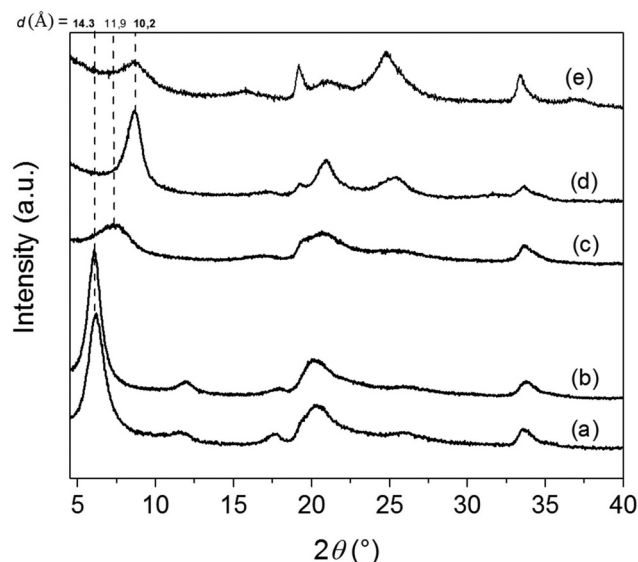
Fig. 4 X-ray powder diffraction patterns of (a) ZrP1$_{1.7}$_1.0; (b) ZrP1$_{1.5}$_1.5; (c) ZrP1$_{1.2}$_3.0; (d) ZrP2$_{0.5}$_3.0; and (e) ZrP2$_{0.4}$_3.6.

should be much higher than the observed ones, since they would derive from the sum of the above values, that is (5.6 + 14.8) Å for ZrP1 and (5.6 + 10.8) Å for ZrP2. (2) Despite the interlayer distance of the compounds being very close to that of pure phosphonates, the absence of the reflection associated with the interlayer distance of Zr(O$_3$PH)$_2$ supports the formation of single-phase mixed compounds in the place of phase separated materials. Moreover, for the ZrP1$_y$_R samples, a reduction of the interlayer distance is observed by decreasing the fraction of phenylphosphonate groups (from 14.3 Å for ZrP1$_{1.7}$_1.0 and ZrP1$_{1.5}$_1.5 to 11.9 Å for ZrP1$_{1.2}$_3.0), suggesting that when the phosphonate/phosphate molar ratio falls below a certain value, the interlayer region tends to "collapse", as a consequence of the possibility of phenyl rings, at

lower phosphonate/phosphate molar ratios, interpenetrating to some extent. This is not possible for ZrP2 materials; due to the presence of rigid pillaring diphosphonates, consistently the interlayer distance did not change with the y value. Considering that, the following models can be proposed for ZrPn materials (Scheme 1).

Fig. 5 shows the FTIR spectra of ZrP1$_{1.5}$_1.5 and ZrP2$_{0.5}$_3.0. Some bands are observed in both materials, specifically, a band at 560 cm^{-1} due to the ν(Zr–O) vibrational mode, bands at 1005 cm^{-1} and 1035 cm^{-1} due to the ν(P–O–Zr) and ν(P–O) vibrational modes, respectively, and a band at 2440 cm^{-1} due to the ν(P–H) of the phosphite group.[12,13] Moreover, the spectrum of ZrP1$_{1.5}$_1.5 exhibits bands at 690, 720, and 750 cm^{-1} due to the out-of-plane bending of the monosubstituted phenyl, a band at 1150 cm^{-1} corresponding to the P–C stretching, bands at 1434 and 1590 cm^{-1} due to the aromatic C=C stretching and a band at 3060 cm^{-1} due to the stretching of the aromatic C–H bond. The spectrum of ZrP2$_{0.5}$_3.0 exhibits a band at 855 cm^{-1} attributable to the out-of-plane bending of the aromatic C–H groups, a band at 1515 cm^{-1} due to the stretching of the aromatic ring, and bands at 1404 cm^{-1} and 2915 cm^{-1} due to the deformation and stretching vibrations of the CH$_2$ group.

Moreover, no broad bands due to water molecules involved in hydrogen bonds were observed above 3100 cm^{-1}. However, ZrP2$_{0.5}$_3.0 shows a small band at about 1260 cm^{-1} (Fig. 5b) that can be attributed to the out-of-plane bending vibration of P–OH; this agrees with the ^{31}P MAS NMR spectrum of ZrP2$_{0.5}$_3.0 (Fig. 1b) that revealed the presence of small amounts of mono and bidentate phosphonate groups with free POH groups, reasonably located on the particle surface and edges.

In the following, the discussion will be focused on ZrP1$_{1.5}$_1.5, ZrP1$_{1.2}$_3.0, ZrP2$_{0.5}$_3.0 and ZrP2$_{0.4}$_3.6.

SEM images of the above samples are shown in Fig. 6–9. At lower magnification, the surface of ZrP2$_{0.5}$_3.0 appears "rougher" and more disaggregated with respect to the others.
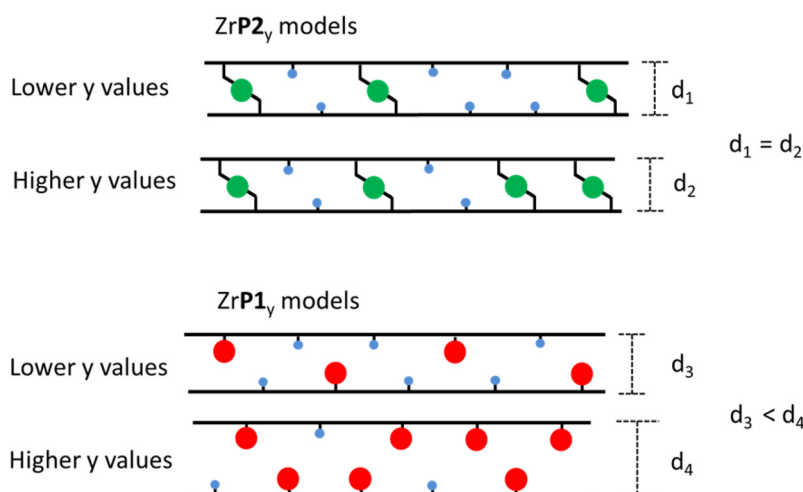
Scheme 1 Representation of the interlayer region of ZrPn materials as a function of the amount of phosphonate groups per mol of Zr (y).

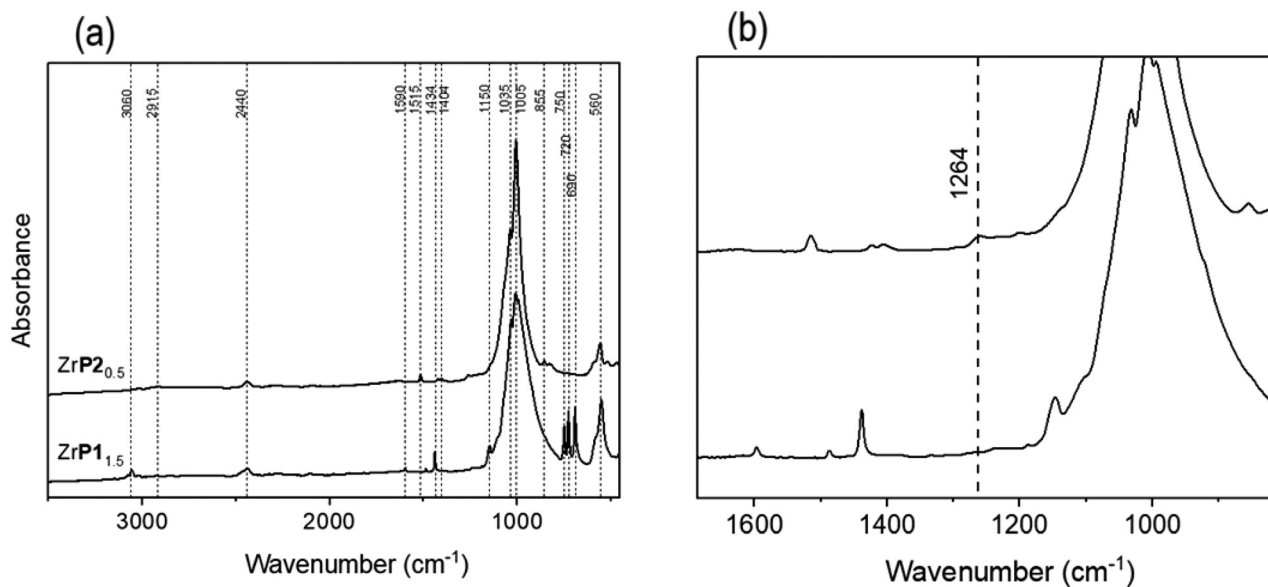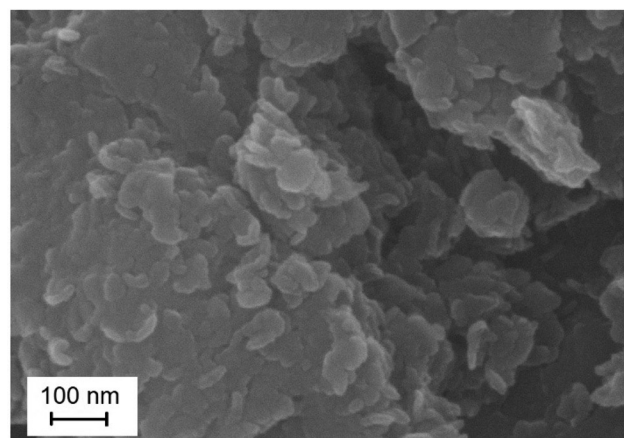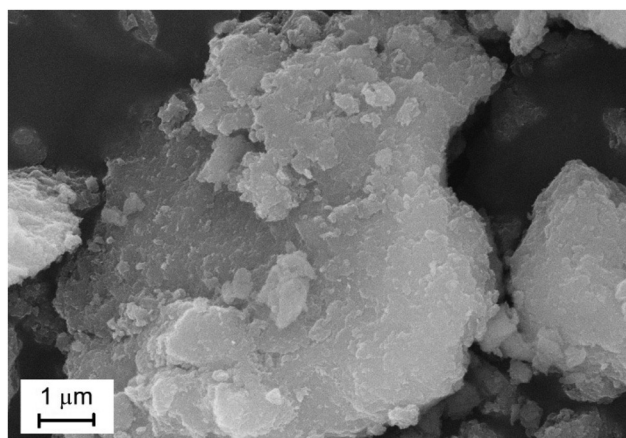**Fig. 5** FTIR spectra of (a) ZrP1$_{1.5}$_1.5 and ZrP2$_{0.5}$_3.0; (b) enlargement of (a).

Fig. 6 SEM images of ZrP1$_{1.2}$_3.0 at different magnifications.
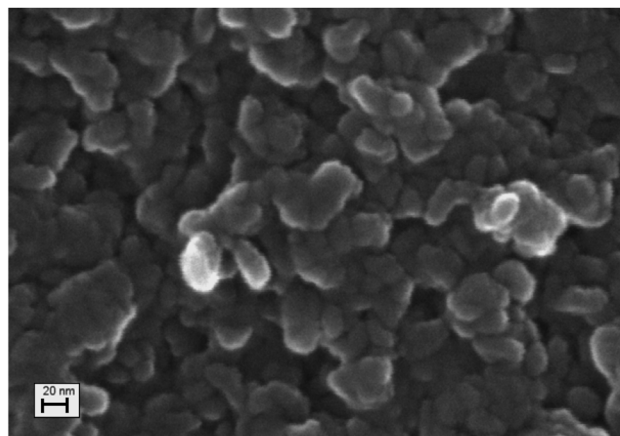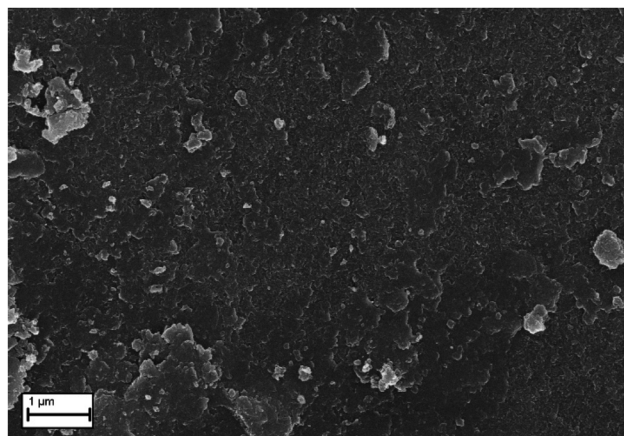

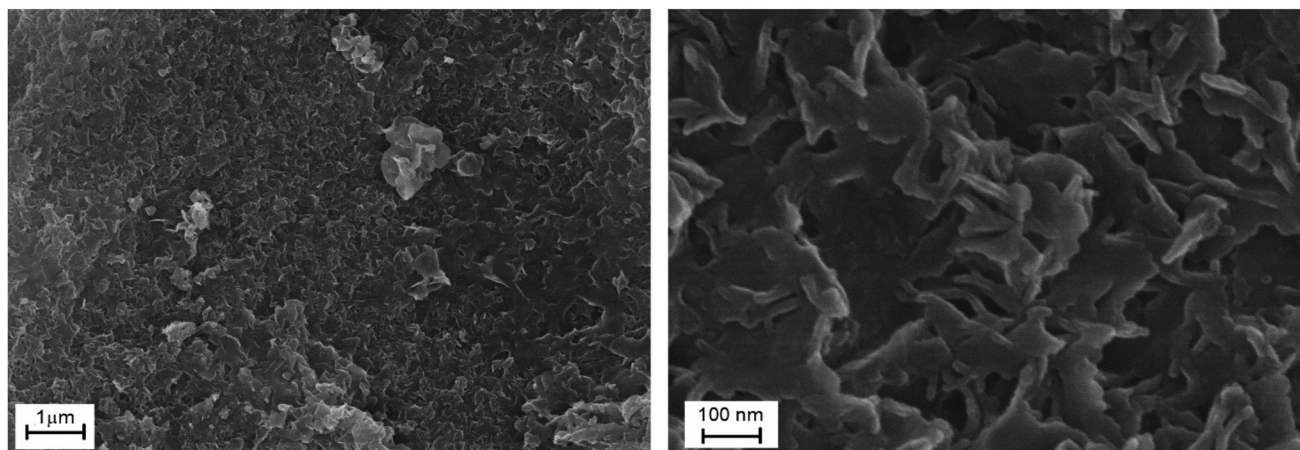**Fig. 7** SEM images of ZrP1$_{1.5}$_1.5 at different magnifications.

Fig. 8 SEM images of ZrP2$_{0.4}$_3.6 at different magnifications.

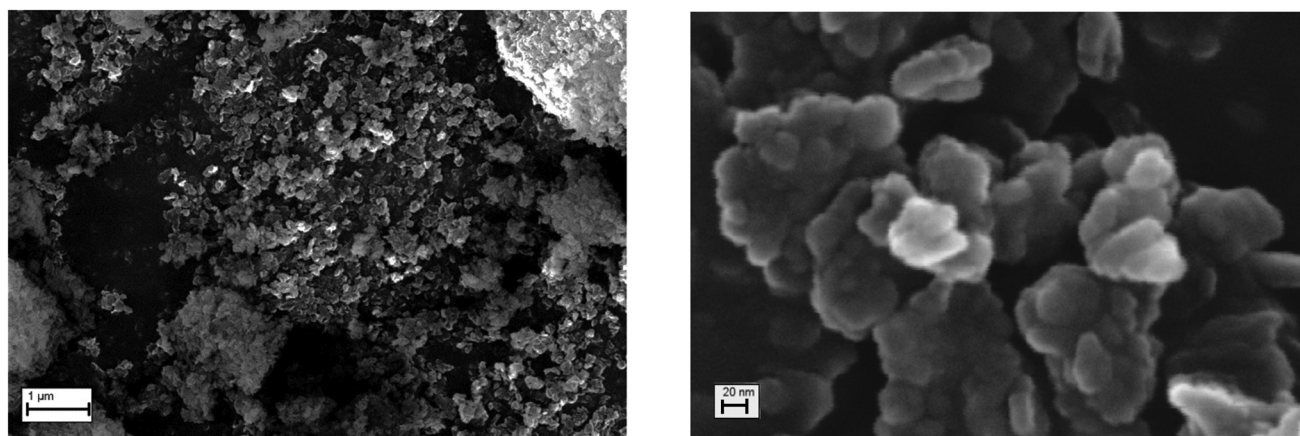**Fig. 9** SEM images of ZrP2$_{0.5}$_3.0 at different magnifications.

Except for **ZrP2**$_{0.4}$_3.6, higher magnification revealed, for all other samples, similar morphologies, consisting of almost round shaped particles with an average size of 20 ± 5 nm, fused or aggregated with each other. The particles of **ZrP2**$_{0.4}$_3.6 are thinner and fused to form a sort of hierarchical network and their average size and thickness are 85 ± 30 nm and 15 ± 5 nm, respectively.

The thermal behaviour of the **ZrP2**$_{0.5}$_3.0 sample in air was tested by thermogravimetry (Fig. 10). The mass reduction at around 200 °C is probably due to the loss of residual moisture and solvent molecules. At temperatures in excess of 350 °C, the exothermal weight gain observed (maximum at 501 °C) can be attributed to the partial oxidation of P–H and/or P–C bonds, giving rise to new P–O and/or C–O bonds. This fact is confirmed by the exothermal nature of the process. Then, the combustion of organic matter occurs with weight losses at higher temperatures.

The N$_2$ adsorption properties of ZrP**n** samples were studied at 77 K and the corresponding adsorption–desorption isotherms are shown in Fig. 11 and 12. The apparent BET specific
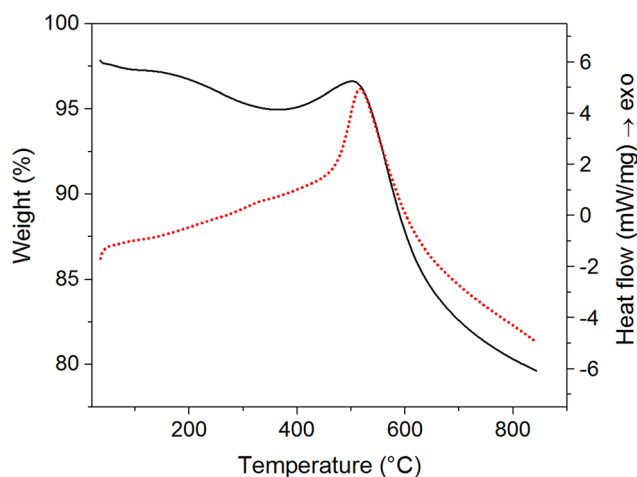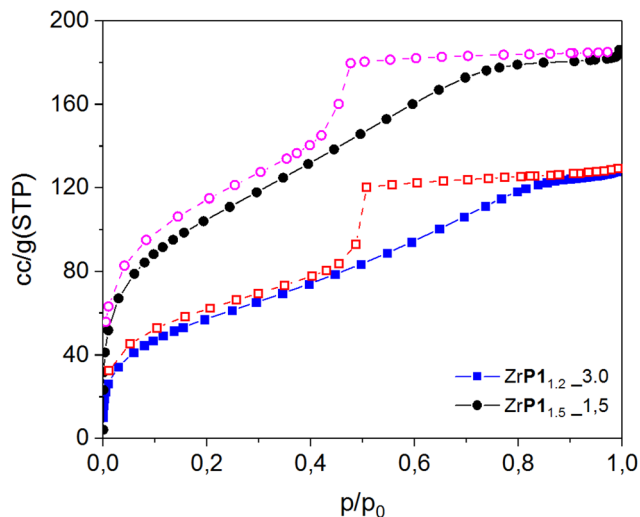

Fig. 10 Thermogram of ZrP2$_{0.5}$_3.0 in air.

Fig. 11 N₂ adsorption (bold symbols) and desorption (hollow symbols) isotherms at 77 K of ZrP1₁.₂_3.0 (squares) and ZrP1₁.₅_1.5 (circles).

Table 3 BET SSA, H₂ uptake and pore volume at 77 K for the Zr**P**n samples

Sample	BET SSA (m² g⁻¹)	H₂ uptake (77 K, 1 atm) (mmol g⁻¹)	V_{micro} (cm³ g⁻¹)	V_{meso} (2–35 nm) (cm³ g⁻¹)	Interlayer distance (Å)
ZrP1₁.₂_3.0	210	0.96	0.040	0.146	11.9
ZrP1₁.₅_1.5	352	1.43	0.082	0.166	14.3
ZrP2₀.₄_3.6	235	1.22	0.042	0.155	10.2
ZrP2₀.₅_3.0	205	0.85	0.039	0.293	10.2

surface areas (SSAs) are reported in Table 3, together with the hydrogen uptake and the pore volume that will be discussed later.

It is noteworthy that, differently from zirconium phosphate phenylphosphonate materials, prepared according to a similar procedure and exhibiting negligible SSA values,[3] Zr**P1**$_y$_R samples display significant specific surface areas and porosities; it is reasonable that the use of phosphoric acid instead of phosphorous acid improves the layer–layer interactions mediated by solvent molecules.

Both Zr**P1**$_y$_R samples (Fig. 11) have a type IV isotherm profile, and the hysteresis indicates the presence of mesopores. The N₂ uptake at low p/p_0 values, larger for Zr**P1**₁.₅_1.5 than for Zr**P1**₁.₂_3.0, is indicative of the presence of micropores. The steep desorption branch for the Zr**P1**$_y$_R samples is a characteristic feature of the H2(a) hysteresis, according to the

IUPAC classification.[14] The hysteresis closure position between 0.5 and 0.4 p/p_0 is due to the percolation desorption in a disordered porous network and/or to a cavitation-induced evaporation occurring in mesopores.[15] The large plateau at relative pressures higher than 0.75 indicates that the mesopores are small enough to be completely filled at relatively low pressures and that macropores are absent.

According to the literature, the Low Pressure Hysteresis (LPH) observed for the two Zr**P1** samples (Fig. 11) may originate from a poor outgassing procedure that is unable to eliminate all of the adsorbed species before the sorption experiments.[16] In order to clarify this point, the N₂ sorption isotherms on the Zr**P1**₁.₅_1.5 and Zr**P1**₁.₂_3.0 samples were obtained after outgassing them at a higher temperature (200 °C). In addition, two hysteresis scanning experiments were performed in sequence to gain a deeper insight into the textural features of the materials (Fig. 13).

The LPH was not suppressed in the sorption–desorption profiles when increasing the pre-treatment of the two samples from 150 to 200 °C; therefore 150 °C is a suitable temperature for the outgassing of the Zr**P1**$_y$_R samples. These results also mean that at 77 K, some N₂ molecules are trapped in strong sorption sites, probably of size comparable to that of nitrogen (3.64 Å). After the complete sorption–desorption measurements (black profiles in Fig. 13), two more sorption–desorption cycles were run within the relative pressure ranges where
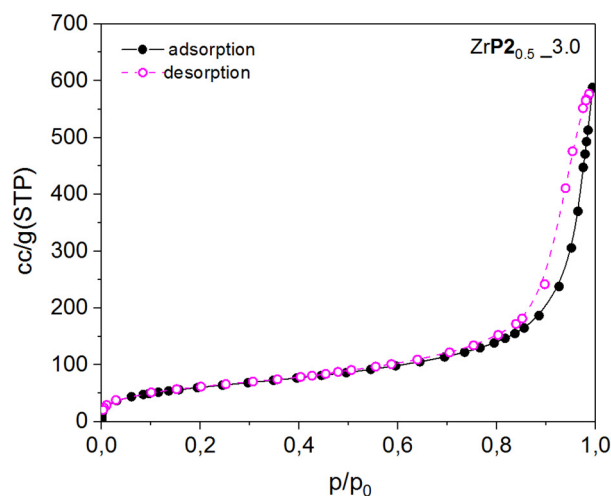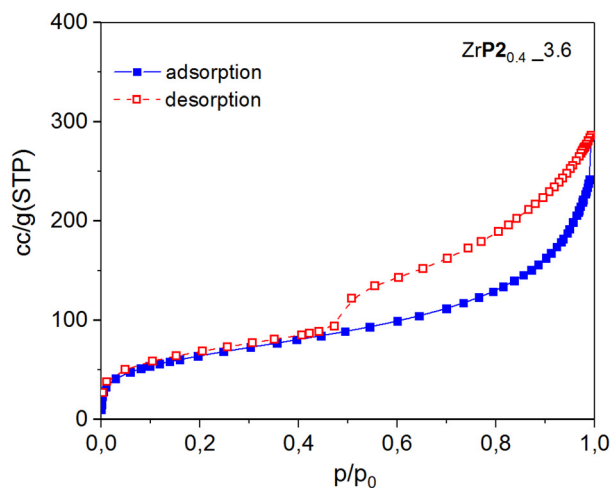

Fig. 12 N₂ adsorption (bold symbols) and desorption (hollow symbols) isotherms at 77 K of ZrP2₀.₄_3.6 (squares) and ZrP2₀.₅_3.0 (circles).
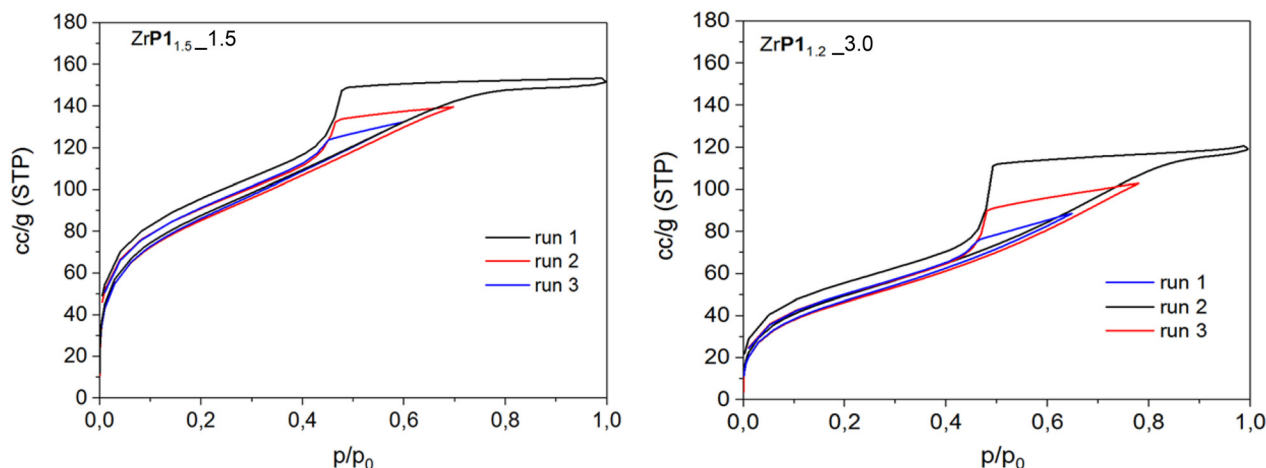
Fig. 13 N_2 hysteresis scanning runs at 77 K of ZrP1$_{1.2}$_3.0 and ZrP1$_{1.5}$_1.5 dried at 200 °C.

hysteresis occurs (red and blue profiles). In this procedure, named a desorption scan, one fills with liquid N_2 only a fraction of the pores. For both materials, the substantially parallel desorption profiles in the hysteresis range indicate that the desorption of the filled mesopores does not depend on the state of neighbouring necks and mesopores. This in turn implies that pore evaporation occurs *via* cavitation only and that the mesopores present in both materials are connected by necks less than 5 nm wide.[17]

The ZrP2$_y$_R samples exhibit a type II adsorption isotherm with a steep nitrogen uptake as saturation is approached (Fig. 12). This behaviour at relative pressures above 0.7 is due to capillary condensation in the inter-particle space or the presence of macropores that are not completely filled.[11] ZrP2$_{0.5}$_3.0 presents a hysteresis loop at p/p_0 values between 0.8 and 1.0, which can be attributed mainly to inter-particle pore condensation. ZrP2$_{0.4}$_3.6 exhibits a pronounced H3 hysteresis loop in the P/P_0 range of 0.5–1.0, which is typical of non-rigid aggregates of plate-like particles and/or of macropores not completely filled with condensate.[14] Indeed, the lower amount of diphosphonic acid in ZrP2$_{0.4}$_3.6, binding together two facing layers, might give rise to more flexible structures. The larger uptake at higher relative pressures when passing from ZrP2$_{0.4}$_3.6 to ZrP2$_{0.5}$_3.0 indicates an enhanced volume adsorbed during capillary condensation and, if macropores are present, an increase of the corresponding pore size.[18]

The pore size distributions and the cumulative pore volumes of the four ZrP1$_y$_R and ZrP2$_y$_R materials were obtained using Micromeritics MicroActive® 6.0 software by fitting the N_2 adsorption isotherms with a non-linear density functional theory (NLDFT) kernel for pillared clays and assuming a cylindrical geometry for the pores. The sorption branch was chosen for all fittings in order to avoid a fictitious peak due to cavitation in the desorption branch. It has to be considered that a pore size distribution below 10–11 Å is not accessible because of the features of the Tristar 3020 II instrument.

The ZrP2$_y$_R samples give rise to major interparticle condensation at high relative pressures (Fig. 11); therefore, the fitting of the isotherms has included all experimental points up to $p/p_0 = 0.95$. The micropore volume (V_{micro}) and the mesopore volume in the range of 2–35 nm (V_{meso}) resulting from the fittings are reported in Table 3.

It is interesting to compare the results obtained in the present work with those obtained by other authors for similar α-type zirconium phosphonates, listed in Table 4.

All of them were prepared by using ZrOCl$_2$·8H$_2$O as a Zr(IV) source and generally using HF as a complexing agent for zirconium or a templating agent, such as CTAB. The procedures employ long times (several days) and temperatures ≥60 °C. These materials are essentially micro- and mesoporous, including inter-crystal mesoporosity.

By plotting the cumulative pore volume as a function of the SSA, the graph presented in Fig. 14 was obtained, showing that most of the samples, including the ZrP1 samples and ZrP2$_{0.4}$_3.6, follow a similar trend, with the pore volume (mainly due to micro- and/or mesopores) almost linearly increasing with increasing SSA. ZrP2$_{0.5}$_3.0 exhibits a high pore volume, considering its SSA. On the basis of the above observations, several conclusions can be drawn on the advantages of the gel method:

• It offers a simple synthetic strategy to obtain α-type zirconium phosphite phosphonates with variable compositions and tunable porous properties, without employing additional compelxing and/or templating agents or long reaction times; in this regard, it is noteworthy that Srinivas *et al.* reported the synthesis of zirconium phosphite phenylphosphonates by using different phosphorous acid/phenylphosphonic acid molar ratios,[22] but they did not observe significant differences in their composition, probably due to the formation of separated phases.

• It allows gelatinous samples to be obtained in organic solvents, retaining a significant amount of solvent that, among other things, can be exchanged with other solvents. As a proof

Table 4 Synthetic conditions, SSA and pore volume of some α-type zirconium phosphonates[a]

P-ligands		Solvent	Complexing/templating agents	Temperature and reaction time	SSA ($m^2 \, g^{-1}$) and pore volume[b] ($cm^3 \, g^{-1}$)	Ref.
1,4-Benzenediphosphonic acid	—	Water ethanol/DMSO	HF	60 °C and 6 days	n.a.	19
				80 °C and 3 days		
	H_3PO_4	Ethanol DMSO	HF	75 °C 6 days	n.a.	19
	H_3PO_3	Water Propanol/water DMSO/water	HF	80 °C and 1 day	405 and 0.52	5
4,4-Biphenylenediphosphonic acid	—	DMSO ethanol/DMSO	HF	80 °C and 3 days	416 and 0.268	20
	H_3PO_4	DMSO	HF		371 and 0.232	20
	$H_2O_3PC_6H_5$	Ethanol/DMSO	HF		396 and 0.293	21
Phenylphosphonic acid	H_3PO_3	Water		90 °C to dryness	439 and n.a.	22
1-Hydroxy ethylidene-1,1′-diphosphonic acid	—	Ethanol/water	CTAB	110 °C and from 0 to 72 h	622 and 0.35	23
3,3′,5,5′-Tetramethylbiphenylenebis (phosphonic acid)	H_3PO_3	DMSO	HF	95 °C	405 and 0.16	5

[a] Zr(IV) source = $ZrOCl_2 \cdot 8H_2O$. [b] Maximum values.
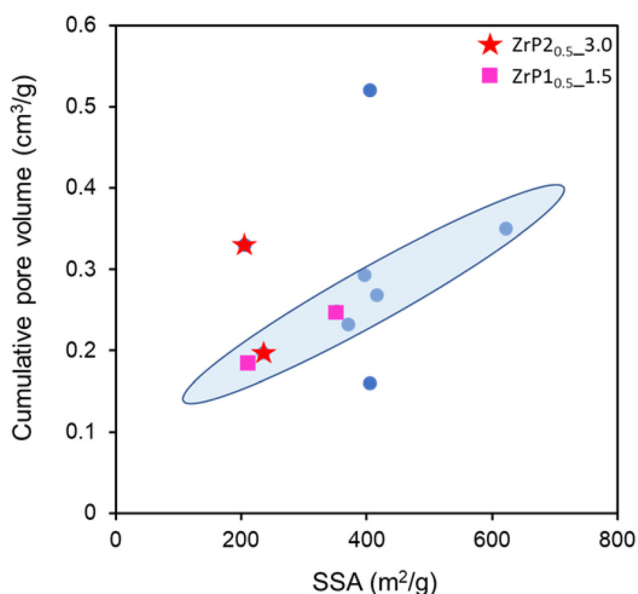
Fig. 14 Cumulative pore volume as a function of the SSA for ZrP1$_{y}$_R, ZrP2$_{y}$_R and the samples listed in Table 4.

of fact, the synthesis of ZrP1$_{1.5}$_1.5 produces a gel in propanol containing 8 mL PrOH per g solid, corresponding to 13.5 wt% of solid in the gel. By washing the gel twice with dichloromethane (DCM), a new gel is obtained containing 7 mL DCM per g solid, corresponding to 10 wt% of solid in the gel. This gel is very useful for the preparation of polymer composites. In order to test the ability of the gel in DCM to disperse in a polymer matrix, composite films were prepared by using a polymer soluble in the same solvent, specifically PLA. Details on the preparation and preliminary characterization of the PLA/ZrP1$_{1.5}$_1.5 composite films are presented in the SI.

The pore size distributions of the two ZrP1$_{y}$_R samples (Fig. S2, SI) and the values of the pore volumes (Table 3) indicate that a larger pore volume is present in the ZrP1$_{1.5}$_1.5 sample with respect to the ZrP1$_{1.2}$_3.0 sample, especially for the smaller pore sizes. This correlates well with its largest planar spacing (14.3 *vs.* 11.9 Å).

The pore size distributions of the two ZrP2 samples (Fig. S3, SI) and the values of the pore volumes (Table 3) indicate a similar pore size distribution for both, up to 60 Å. The number of pores of larger size is higher in the ZrP2$_{0.5}$_3.0 sample with respect to the ZrP2$_{0.4}$_3.6 sample, even though the planar spacing (10.2 Å) is the same for both samples, as evidenced by the larger uptake of N_2 at saturation (Fig. 12) and by the larger V_{meso} value in Table 3.

The hydrogen adsorption isotherms measured at 77 K are shown in Fig. 15 and 16. Both materials display a type I isotherm with a hysteresis loop and no saturation uptake was observed under the selected experimental conditions. As reported by several authors, hysteresis during hydrogen adsorption/desorption can be due, among other factors, to surface heterogeneity and the presence of defects.[24]

The H_2 uptake at 77 K, calculated from the adsorption isotherms at 1 atm, is reported in Table 3. As a general trend, the hydrogen uptake increases with increasing SSA and, in turn, with increasing micropore volume, and among all materials, ZrP1$_{1.5}$_1.5 showed the highest hydrogen uptake.

By comparing the micropore volume with the average interlayer distances, it is observed that for the ZrP1$_{y}$_R materials, the micropore volume increases with increasing interlayer distance, while for the ZrP2$_{y}$_R materials, the micropore volume increases slightly when passing from ZrP2$_{0.5}$_3.0 to ZrP2$_{0.4}$_3.6, with the interlayer distance being the same.

Our results are consistent with the models reported in Scheme 1, when assuming the contribution of the interlayer
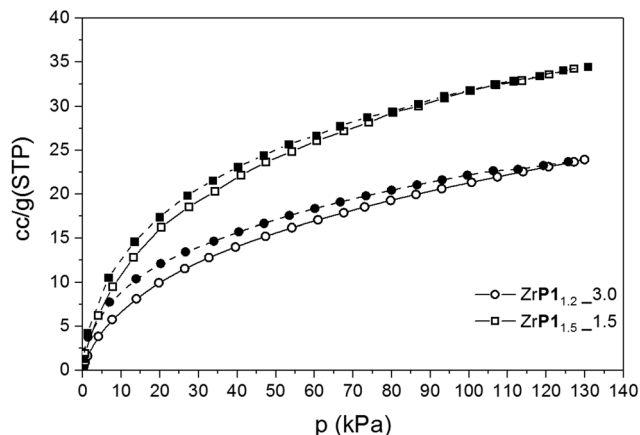
Fig. 15 H_2 adsorption (hollow symbols) and desorption (bold symbols) isotherms at 77 K of ZrP1$_{1.2}$_3.0 (circles) and ZrP1$_{1.5}$_1.5 (squares).

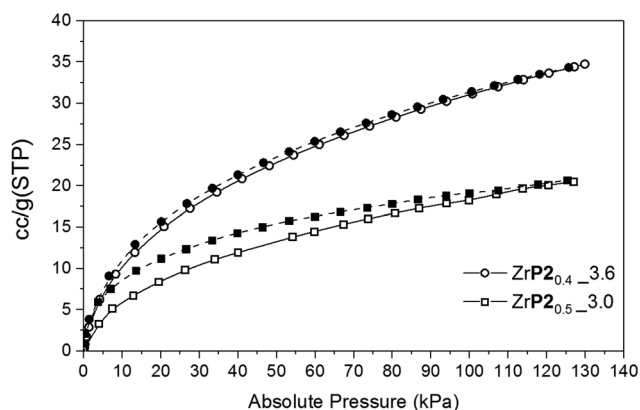**Fig. 16** H_2 adsorption (hollow symbols) and desorption (bold symbols) isotherms at 77 K of ZrP2$_{0.4}$_3.6 (circles) and ZrP2$_{0.5}$_3.0 (squares).

free space to microporosity. For the ZrP2$_y$_R materials, the interlayer distance is independent of the y value, so a higher free interlayer space is expected at lower y values, supporting the higher micropore volume and hydrogen uptake when passing from ZrP2$_{0.5}$_3.0 to ZrP2$_{0.4}$_3.6. Differently, for the ZrP1$_y$_R materials, a decrease of the y value corresponds to a decrease of the interlayer distance as a consequence of the formation of an interpenetrated structure, which probably reduces the interlayer free volume.

As reported by Alberti and Clearfield,[5,7] a house-of-cards structure can be assumed for the ZrP1$_y$ and ZrP2$_y$ materials, supported by edge–edge interactions between the layer packets that should be further sustained by the presence of diphosphonate groups and could justify the presence of low coordinated phosphonate groups, as schematically illustrated in Fig. 17.

A further evaluation of the adsorption properties was performed toward VOCs; due to the presence of hydrophobic functional groups, the capacity of the above materials to take up low polarity volatile solvents was investigated and dichloromethane (DCM) was chosen as the model solvent. Uptake tests by the vapor phase were carried out at 30 °C under saturation con-
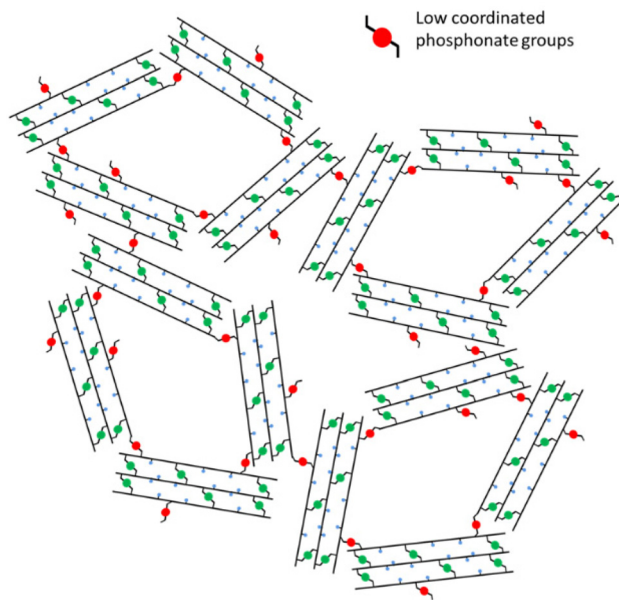

Fig. 17 Schematic representation of the possible house-of-cards structure of ZrP2$_y$_R materials.

ditions. In light of its larger SSA, ZrP1$_{1.5}$_1.5 was selected for this study and compared with ZrP2$_{0.5}$_3.0, exhibiting the lowest SSA. The DCM uptake as a function of time is shown in Fig. 18.

The DCM amount after 160 hours was ~400 mg g^{-1} of solid and 1300 mg g^{-1} of solid for ZrP1$_{1.5}$_1.5 and ZrP2$_{0.5}$_3.0, respectively. Despite ZrP1$_{1.5}$_1.5 exhibiting the largest SSA, it absorbs less DCM than ZrP2$_{0.5}$_3.0. The different DCM adsorption capacities correlate instead with the larger macroporous volume evidenced by the N_2 sorption isotherms for ZrP2$_{0.5}$ than for ZrP1$_{1.5}$ (Fig. 11 and 12). The approximate volumes occupied at 77 K by N_2 and by dichloromethane at 30 °C, both at saturation, have been estimated through the liquid density

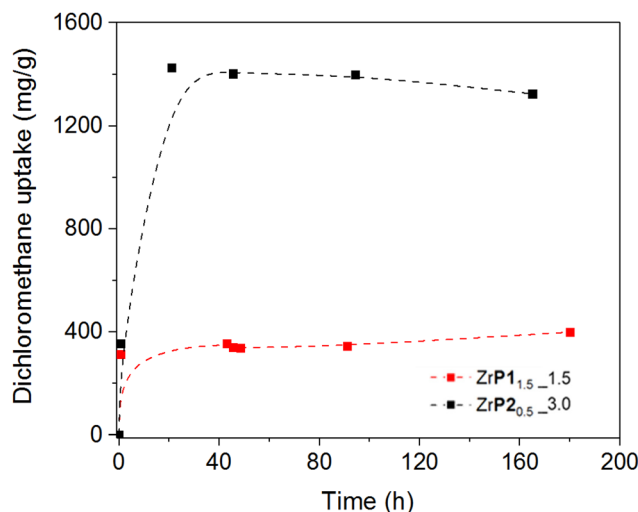**Fig. 18** Dichloromethane uptake as a function of time for ZrP1$_{1.5}$_1.5 and ZrP2$_{0.5}$_3.0 at 30 °C under saturation conditions.

of the two fluids, namely 0.806 g cm^{-3} for liquid N$_2$ and 1.3087 g cm^{-3} for dichloromethane at 30 °C.[25] When liquid N$_2$ is considered, these volumes are 0.835 and 0.264 cm^3 g^{-1} for ZrP2$_{0.5}$ and ZrP1$_{1.5}$, respectively. Using dichloromethane at 30 °C, these values are 0.993 and 0.306 cm^3 g^{-1}, with increases of 16% and 19%, respectively. There is no correlation with the micropore volume (Table 3); instead, mesopores, macropores and interparticle porosity play a determining role in the DCM uptake.

It is interesting to compare these results with those obtained for other porous materials, such as MOFs, zeolites and activated carbons.[26–34] A list of some inorganic sorbents is reported in Table S1, SI. The maximum uptake of DCM was plotted as a function of the pore volume and the corresponding graph is shown in Fig. 19. The materials included in the blue region are almost microporous; for example, Chen found a DCM adsorption amount of 13.12 mmol g^{-1} (1115 mg g^{-1}) for HKUST-1 at 298 K (SSA = 0.81 cm^3 g^{-1}).[26] The result was attributed to the contribution of two kinds of pores, having diameters of 9.0 Å and 5.0 Å, which are larger than the kinetic diameter of DCM (3.3 Å); as a proof of facts, the same material exhibits a lower trichloromethane adsorption capacity, with its kinetic diameter being 6.5 Å, so that only the largest pores of HKUST-1 are involved in the adsorption. The points included in the yellow area refer to carbon-based materials and exhibit a lower DCM uptake with respect to other sorbents with similar pore volumes.[30,34] Differently, ZrP2$_{0.5}$_3.0 and the XAD-1600 resin (green area of the graph), both characterized by macroporosity, exhibit a higher DCM uptake with respect to other sorbents with similar pore volumes.[31] Many factors affect the above results (measurement conditions, pore size and amount, and chemical composition, among others) and their interpretation is anything but trivial.
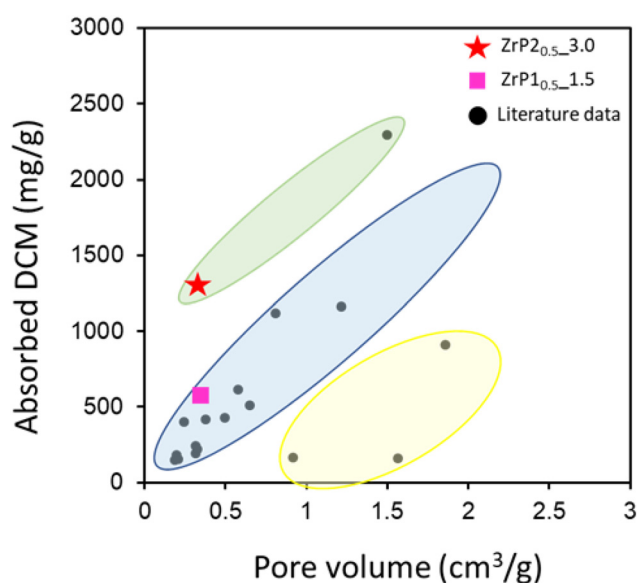
In this regard, it should be considered that the DCM uptake measurements of most of the considered sorbent materials[26–34] are carried out under conditions different from those reported in the present work. For instance, a gravimetric analyzer is frequently used; the sample is vacuumed to low pressures and outgassed to remove any residual guests, the adsorbed water or gases. Nevertheless, the contribution due to macroporosity to the significant DCM uptake observed for ZrP2$_{0.5}$_3.0 should not be ignored. We tried to reuse the ZrP2$_{0.5}$_3.0 sample by drying it in an oven at 100 °C for 1 hour and then contacting it again with DCM vapor at 30 °C. The dichloromethane uptake at equilibrium, after 91 hours, was 1439 mg g^{-1} of solid.

4. Conclusions

Single-phase mixed zirconium phosphite phosphonate materials with layered and pillared structures were easily prepared by the gel method. By varying the phosphorous acid/phosphonic acid molar ratio in the reaction solutions, materials with different chemical compositions were prepared, which exhibit significant specific surface areas. By changing both the nature of the phosphonate group and the phosphite/phosphate molar ratio, different micro/meso/microporous structures were obtained that affect their adsorption capabilities. In particular, they proved to be competitive with MOFs toward dichloromethane adsorption. Thanks to the encouraging results obtained for the mechanochemical synthesis of nanosized α-type zirconium phosphate,[11] we are currently studying the possibility of applying the same technique to the synthesis of porous zirconium phosphite phosphonate materials without using solvents. Moreover, the above materials are promising as fillers for hydrophobic polymers. In particular, future tests will be devoted to their use for the preparation of mixed matrix membranes based on polymers of intrinsic microporosity in order to test the effect of different polymer–filler interfaces on the transport properties and the physico-chemical features of the membranes.

Conflicts of interest

The authors declare no conflicts of interest.

Data availability

The datasets generated and/or analysed in the current study are available from the corresponding author upon reasonable request. All relevant data supporting the findings of this study are included within the article.

Supplementary information (SI) is available. ^{31}P MAS and CPMAS NMR spectra, pore size distributions, DCM uptake and SSA of some porous absorbent materials, synthesis of PLA/ZrP1$_{1.5}$_1.5 composite films and their preliminary characterization. See DOI: https://doi.org/10.1039/d5dt02320c.

Fig. 19 DCM capacity as a function of the pore volume for some micro-, macro- and mesoporous materials listed in Table S1.

Acknowledgements

References

1 A. Clearfield and U. Costantino, in *Comprehensive Supramolecular Chemistry*, ed. G. Alberti and T. Bein, Pergamon, Elsevier Science Ltd., New York, 1996, vol. 7, pp. 145–176.

2 M. Pica, A. Donnadio, D. Capitani, R. Vivani, E. Troni and M. Casciola, *Inorg. Chem.*, 2011, **50**, 11623–11630.

3 M. Pica, A. Donnadio, R. D'Amato, D. Capitani, M. Taddei and M. Casciola, *Inorg. Chem.*, 2014, **53**, 2222–2229.

4 M. Pica, A. Donnadio, E. Troni, D. Capitani and M. Casciola, *Inorg. Chem.*, 2013, **52**, 7680–7687.

5 G. Alberti, R. Vivani, F. Marmottini and P. Zappelli, *J. Porous Mater.*, 1998, **5**, 221–226.

6 G. Alberti, U. Costantino, F. Marmottini, R. Vivani and P. Zappelli, *Microporous Mesoporous Mater.*, 1998, **21**, 297–304.

7 A. Clearfield, *Chem. Mater.*, 1998, **10**, 2801–2810.

8 A. Clearfield and Z. Wang, *J. Chem. Soc., Dalton Trans.*, 2002, 2937–2947.

9 (*a*) P. Varhadi, M. Kotwal and D. Srinivas, *Appl. Catal., A*, 2013, **462**, 129–136; (*b*) F. Odobel, B. Bujoli and D. Massiot, *Chem. Mater.*, 2001, **13**, 163–173; (*c*) B. Louis, L. Delmotte, J.-C. Jumas, J.-F. Paul, J.-L. Bonardet, J.-F. Lambert and J.-C. Lavalley, *J. Mol. Struct.*, 2003, **651–653**, 427–435.

10 M. Casciola, D. Capitani, A. Comite, A. Donnadio, V. Frittella, M. Pica, M. Sganappa and A. Varzi, *Fuel Cells*, 2008, **8**(3–4), 217–224.

11 R. Vivani, L. Trovarelli, M. S. Notari, G. Paul, G. Gatti, E. De Paolis and M. Pica, *J. Phys. Chem. C*, 2025, **129**(34), 15480–15487.

12 Y. A. Karavanova, D. V. Golubenko and A. B. Yaroslavtsev, *Membr. Membr. Technol.*, 2020, **2**, 251–255.

13 A. Contreras-Ramirez, B. E. Tomlin, G. S. Day, A. Clearfield and H.-C. Zhou, *Chem. – Eur. J.*, 2020, **26**, 6185–6192.

14 M. Thommes, K. Kaneko, A. V. Neimark, J. P. Olivier, F. Rodriguez-Reinoso, J. Rouquerol and K. S. W. Sing, *Pure Appl. Chem.*, 2015, **87**, 1051–1069.

15 K. A. Cychosz, R. Guillet-Nicolas, J. García-Martínez and M. Thommes, *Chem. Soc. Rev.*, 2017, **46**, 389–414.

16 T. Zelenka, *et al.*, *Small*, 2024, **22**, 2311990.

17 C. Schlumberger and M. Thommes, *Adv. Mater. Interfaces*, 2021, **8**, 2002181.

18 W. C. Li, A. H. Lu, C. Weidenthaler and F. Schüth, *Chem. Mater.*, 2004, **16**, 5676–5681.

19 A. Clearfield, Z. Wang and P. Bellinghausen, *J. Solid State Chem.*, 2002, **167**, 376–385.

20 Z. Wang, J. M. Heising and A. Clearfield, *J. Am. Chem. Soc.*, 2003, **125**(34), 10375–10383.

21 A. Clearfield, *Dalton Trans.*, 2008, (44), 6089–6102.

22 P. Varhadi, M. Kotwal and D. Srinivas, *Appl. Catal., A*, 2013, **462**, 129–136.

23 X. Z. Lin and Z. Y. Yuan, *RSC Adv.*, 2014, **4**(61), 32443–32450.

24 M. S. L. Hudson, H. Raghubanshi, S. Awasthi, T. Sadhasivam, A. Bhatnager, S. Simizu and O. N. Srivastava, *Int. J. Hydrogen Energy*, 2014, **39**, 8311–8320.

25 R. L. Rowley, W. V. Wilding, J. L. Oscarson, Y. Yang, N. A. Zundel, T. E. Daubert and R. P. Danner, *DIPPR® Data Compilation of Pure Chemical Properties*, Design Institute for Physical Properties, AIChE, New York, 2007.

26 F. Tian, X. Zhang and Y. Chen, *RSC Adv.*, 2016, **6**, 31214–31224.

27 L. Zhou, X. Zhang and Y. Chen, *Mater. Lett.*, 2017, **197**, 167–170.

28 N. Missaoui, B. Gassoumi, S. Nasr, H. Kaur, A. Karayel, E. A. Lopez-Maldonado, *et al.*, *J. Mol. Liq.*, 2025, **418**, 126716.

29 Y. Zhou, L. Zhou, X. Zhang and Y. Chen, *Microporous Mesoporous Mater.*, 2016, **225**, 488–493.

30 S. Liu, S. Wu, M. Li, Y. Li and X. Wang, *Ind. Crops Prod.*, 2024, **209**, 118053.

31 J. W. Lee, H. J. Jung, D. H. Kwak and P. G. Chung, *Water Res.*, 2005, **39**, 617–629.

32 S. H. Hsu, C. S. Huang, T. W. Chung and S. Gao, *J. Taiwan Inst. Chem. Eng.*, 2014, **45**(5), 2526–2530.

33 H. Zhang, Y. Zheng, Q. Ren, E. O. Fagbohun and Y. Cui, *Sep. Purif. Technol.*, 2025, **360**, 130889.

34 S. Kang, J. Ma, Q. Wu and H. Deng, *J. Chem. Eng. Data*, 2018, **63**(6), 2211–2218.